Magnetic Resonance Letters 3 (2023) 286–297

Contents lists available at ScienceDirect

Magnetic Resonance Letters

journal homepage: www.keaipublishing.com/MRL

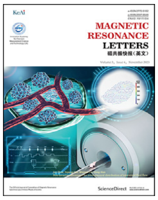

Research Article

Non-invasive assessment for intratumoural distribution of interstitial fluid flow

Jun Zhao [a, b, #], Yupeng Cao [a, #], Wentao Liu [a, b, *], Dong Han [a, b, **]

[a] *CAS Center for Excellence in Nanoscience, National Center for Nanoscience and Technology, Beijing, 100190, China*
[b] *School of Future Technology, University of Chinese Academy of Sciences, Beijing, 100049, China*

ARTICLE INFO

Article history:
Received 17 November 2022
Received in revised form 18 February 2023
Accepted 3 March 2023
Available online 16 March 2023

Keywords:
Interstitial fluid flow
Interstitial flow velocity-MRI
Losartan
Slow flows
Tumour microenvironment

ABSTRACT

Interstitial fluid plays a vital role in drug delivery and tumour treatment. However, few non-invasive measurement methods are available for measuring low-velocity biological fluid flow. Therefore, this study aimed to develop a novel technology called interstitial flow velocity-MRI. The interstitial flow velocity-MRI sequence consists of a dual inversion recovery preparation and an improved stimulated echo sequence (ISTE) combined with phase-contrast MRI. A homemade flow phantom was used to assess the feasibility and sensitivity of interstitial flow velocity-MRI. In addition, xenografts of female BALB/c mouse models of 4T1 breast cancer administered losartan (40 mg/kg) or saline ($n = 6$) were subjected to imaging on a 7.0 T scanner to assess the *in vivo* interstitial fluid flow velocity. The results showed a significant correlation ($P < 0.001$) between the theoretical velocities and velocities measured using the flow phantom. Interstitial flow velocity-MRI could detect a velocity as low as 10.21 ± 2.65 μm/s with a spatial resolution of 0.313 mm. The losartan group had a lower mean interstitial fluid velocity than the control group (85 ± 16 *vs* 113 ± 24 μm/s). In addition, compared to the saline treatment, losartan treatment reduced the proportion of collagen fibres by 10% and 12% in the Masson and Sirius red staining groups, respectively. Interstitial flow velocity-MRI has the potential to determine interstitial fluid flow velocity non-invasively and exhibits an intuitive velocity map.

1. Introduction

Interstitial fluid flow is closely related to drug delivery and distribution, playing a crucial role in their therapeutic effects on tumours [1–3]. It affects macromolecular drugs such as nanoparticles [4,5] more than diffusion-restricted small-molecule drugs, potentially hindering transport and uneven distribution throughout the tumour [6]. Because we currently lack satisfactory methods to measure interstitial fluid flow, we cannot achieve a more comprehensive understanding of the tumour microenvironment. As a result, early diagnosis of tumours and the development of anti-tumour drugs are hampered [7,8].

---

[*] Corresponding author. CAS Center for Excellence in Nanoscience, National Center for Nanoscience and Technology, Beijing, 100190, China.
[**] Corresponding author. CAS Center for Excellence in Nanoscience, National Center for Nanoscience and Technology, Beijing, 100190, China.
E-mail addresses: liuwentao@nanoctr.cn (W. Liu), dhan@nanoctr.cn (D. Han).

[#] These authors contributed equally to the article.

Peer review under responsibility of Innovation Academy for Precision Measurement Science and Technology (APM), CAS.

https://doi.org/10.1016/j.mrl.2023.03.001

Abbreviations

ISTE	improved stimulated echo sequence
MRI	magnetic resonance imaging
FRAP	fluorescence recovery after photobleaching
OCT	optical coherence tomography
DCE	dynamic contrast enhancement
PC-MRI	phase-contrast MRI
TE	echo time
SNR	signal-to-noise ratio
SE	spin echo
STE	stimulated echo
RF	radio frequency
ID	inner diameter
TR	repetition time
FA	flip angle
FOV	field of view
EPl	echo planar imaging

Interstitial fluid flow velocity is most often measured using fluorescence recovery after photobleaching (FRAP) [9,10] or optical coherence tomography (OCT) techniques [11]. These two methods are difficult to use for measuring deep interstitial fluid velocity, which is measured by dynamic contrast enhancement (DCE) instead [12,13]. DCE alters organisms' natural flow by introducing tracers by invasion. Phase-contrast MRI (PC-MRI) is another widely used technology for measuring the velocity of rapid flow in biological tissues, such as blood [14,15]. It does not involve exogenous tracers and allows direct velocity measurements in deep tissue.

Conventional PC-MRI mainly aims to image fast-flowing fluids such as blood, usually using gradient echo sequences. However, when slow-flow imaging significantly increases the echo time (TE), the signal is dramatically affected by the T_2* effect, and the image signal-to-noise ratio (SNR) is severely weakened. In contrast to the gradient echo sequence, the spin echo (SE) sequence uses a 180° focusing pulse to focus the signal in the transverse plane, and its signal is affected by T_2 relaxation, which decays more slowly and has a slightly higher image SNR than T_2* relaxation. A stimulated echo (STE) sequence, which excites a part of the signal to the longitudinal plane, can mitigate part of the T_2 relaxation decay. However, STE is not superior to SE under any TE condition, and there is an urgent need for a method to minimize the effect of T_2 relaxation attenuation on the signal for slow-flow imaging.

The interstitial fluid velocity is four orders of magnitude lower than blood flow (arterial blood velocity of approximately 5–70 cm/s and venous blood velocity of approximately 1.5–28 cm/s) [1]. PC-MRI requires considerable gradient intensity and duration if used for slow flow measurements [16], but high gradient intensity is particularly sensitive to motion and tends to produce motion artifacts during imaging. In addition, when measuring slow flow velocity, the encoding gradient is large, and the TE is relatively long. The SNR is significantly lost because the gradient echo is based on T_2* relaxation decay. In particular, a high slew rate will cause intense peripheral nerve stimulation when applied to living organisms, especially humans. Therefore, PC-MRI clinical application will be greatly limited.

In this study, we developed a novel interstitial flow velocity-MRI sequence. Our method combines PC-MRI with a double-inversion recovery preparation designed to eliminate blood flow signals and an improved stimulation echo sequence (ISTE). Dual inversion [17,18], velocity encoding [19], and ISTE [20] have been used separately in other contexts. Combining these three techniques is a novel approach for measuring interstitial fluid flow *in vivo* (see Fig. 1 for a flow chart of the process). In addition, ISTE can better minimize the influence of T_2 relaxation attenuation on signals [16], motion artifacts, and slew rate than SE and STE sequences [20].

Losartan is an approved angiotensin system inhibitor with notable antifibrotic activity and has been clinically approved to control hypertension. Frimpong et al. reported that losartan inhibits the synthesis of collagen I in tumours [21]. Vikash et al. have found that losartan reduces solid stress in tumours, resulting in increased vascular perfusion [22]. Wende et al. suggested that combining losartan with radiotherapy can be a new therapeutic strategy for desmoplastic tumours [23]. However, the effect of losartan on interstitial fluid has not been reported.

This study describes an *in vivo* and non-invasive imaging technique for mapping mouse interstitial fluid flow velocity and spatial distribution. This non-invasive and quantitative method provides a deeper understanding of the tumour interstitial fluid. In addition, it helps to understand the effect of losartan on the tumour microenvironment, which can also be used to rapidly screen other drugs that alter the flow velocity of interstitial fluid.

2. Methods

2.1. Theory

Phase images have spurious errors due to field inhomogeneities or RF penetration effects. These background phases are independent of the bipolar gradient pulse and can be eliminated if two images are collected and subtracted. Change in polarity or magnitude of the bipolar gradient lobes between such two scans yields velocity-dependent phase information in the subtracted image [24].

By designing an appropriate gradient waveform, such as a bipolar pair or a pair of gradients of the same polarity on either side of a π pulse, the phase differences, $\Delta\Phi$, of the two velocity encoding gradients can be depicted as equations (1) and (2), including the gyromagnetic ratio γ, velocity encoding gradient area m, the interval $\varDelta$ between the velocity encoding gradient, the fluid flow velocity υ, the velocity encoding gradient duration time δ, bipolar gradient G, and time t. As shown in equation (3), the fluid flow velocity can be calculated from the phase differences, the gyromagnetic ratio, the velocity encoding gradient area, and the interval between the velocity encoding gradient [25].

$$\Delta\Phi = 2\gamma m \varDelta \upsilon, \tag{1}$$

$$m = \int_0^{\delta} G\mathrm{d}t, \tag{2}$$

$$\upsilon = \frac{\Delta\Phi}{2\gamma m \varDelta}. \tag{3}$$

The value of the phase map of magnetic resonance appears as -π to π, and the sensitivity of the phase measurement of flow velocity can be expressed as equation (4). Therefore, the minimum resolvable velocity is determined by the product of the two parameters velocity encoding gradient area m and the interval $\varDelta$ between the velocity encoding gradient.

$$\frac{\mathrm{d}\Delta\Phi}{\mathrm{d}\upsilon} = 2\gamma m \varDelta. \tag{4}$$

This study combined the velocity encoding gradient with the ISTE sequence (Fig. 1A). Velocity encoding gradients with the same area and shape on the sides of the second and fourth pulses result in a phase change. The second velocity encoding gradient, marked using the dashed portion, is mirror-symmetrical to the first velocity encoding gradient, resulting in another phase change. The phase unwrapping method was proposed by Liu et al. [26].

The ISTE is shown in Fig. 1A, where the signal is excited from the transverse plane to the longitudinal plane and then a 180° pulse is used to refocus the signal in the longitudinal plane before it is excited to the transverse plane for imaging. This method minimizes the effect of T_2 relaxation decay on the signal as compared to SE and STE sequences. The development of slow-flow imaging based on this method can optimize the image SNR [20].

Equations (5) and (6) express that the signal strength is also subject to signal attenuation caused by diffusion gradient.

$$S = e^{-bD} S_{\mathrm{ISTE}}, \tag{5}$$

$$b = \gamma^2 G^2 \delta^2 \left(\varDelta - \frac{\delta}{3}\right). \tag{6}$$

where S is the signal of ISTE after diffusion attenuation effect due to velocity encoding gradient, S_{ISTE} is the signal of ISTE, b is the diffusion sensitivity factor, D is the diffusion coefficient, and δ is the velocity encoding gradient duration time.

According to equation (4), the minimum resolvable velocity is determined by the product of the two parameters velocity encoding gradient area m and the interval $\varDelta$ between the velocity encoding gradient. When the minimum solvable velocity is constant, m is inversely proportional to $\varDelta$. When the velocity gradient is rectangular, equation (2) can be approximated as $m = G\delta$. According to equations (2) and (6), $b = \gamma^2 m^2 (\varDelta - \frac{\delta}{3})$, $\varDelta$ increases linearly, and m decreases by the square, which causes b to decrease. Therefore, our work increased the gradient interval $\varDelta$, which can minimize the b value under the same flow velocity measurement sensitivity, thereby reducing the signal loss caused by diffusion and improving the detection accuracy of slow-flow imaging.

The velocity range of interstitial fluid velocity is estimated to be no more than 500 μm/s. Flow weighting is characterized by the user-controlled velocity encoding *anti*-aliasing factor, *Venc*, which for a given flow-encoding gradient is the velocity at which the phase begins to wrap to $\pm\pi$ [25]. From equations (3) and (7), the values of parameters m and $\varDelta$ are optimized and adjusted as *Venc* to improve the accuracy of slow-flow imaging.

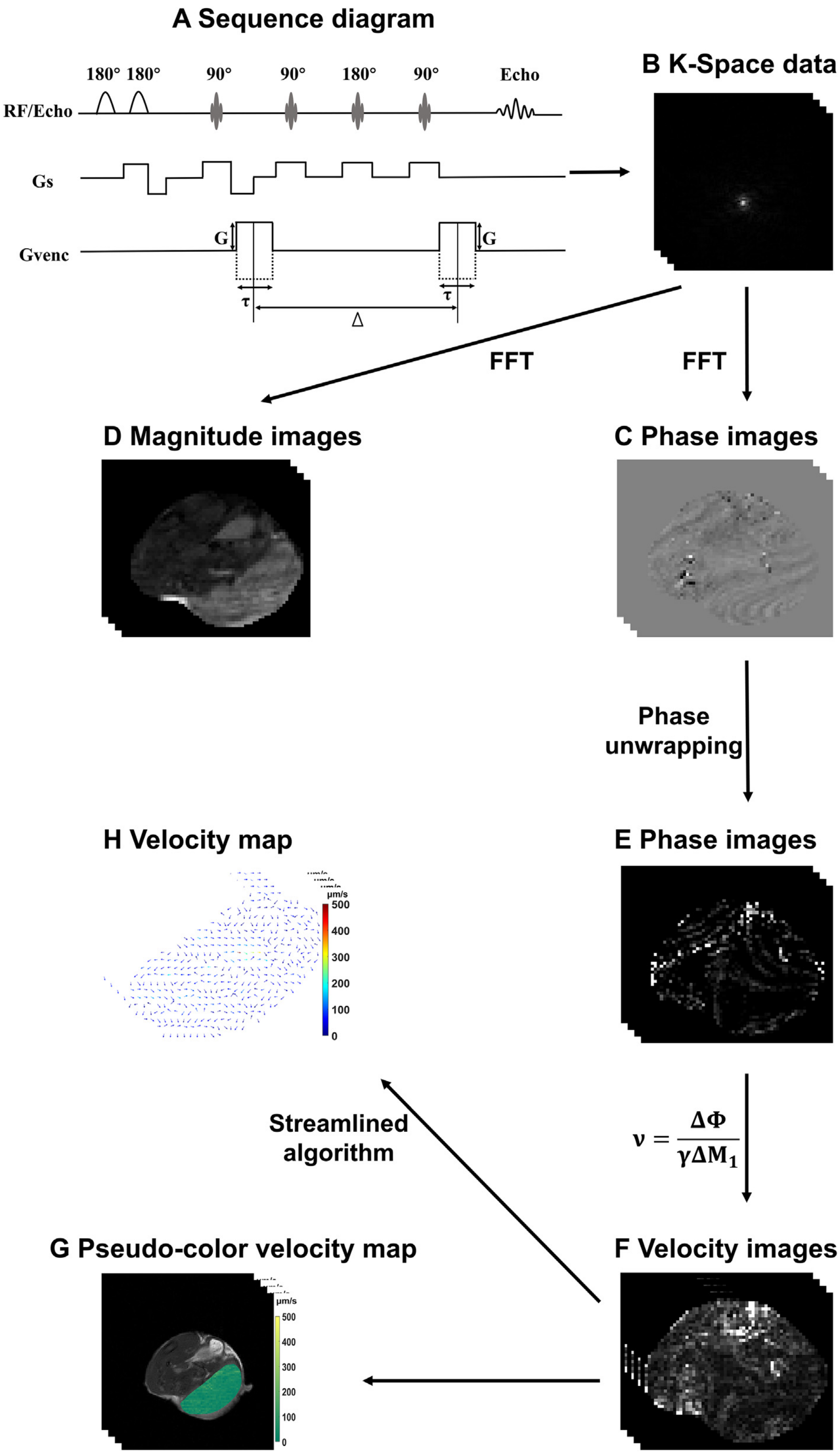

Fig. 1. Schematic diagram of interstitial liquid velocity measurement and data processing. A sequence diagram for the interstitial flow velocity-MRI (A). Representative image of *k*-space (B), phase image obtained by Fourier transform (C), magnitude image obtained by Fourier transform (D), phase image obtained after unwrapping (E), velocity image (F), pseudo-color image (G). The color velocity vector diagram obtained by the streamlined algorithm (H).

$$Venc = \frac{\pi}{\gamma m \Delta}. \tag{7}$$

where γ is the gyromagnetic ratio of the nuclei.

In tumour interstitial fluid slow-flow imaging, which is affected by blood flow, this study used two or more inversion pulses to suppress the blood flow signal. The first uses a non-selected layer of 180° pulses, followed by a selected layer of 180° pulses so that the blood flow signal within the layer is inverted, and after a TI (blood signal over zero time), a 90° excitation is performed. This double inversion pulse can be performed several times to enhance blood signal suppression [25].

2.2. MRI measurements

The imaging was performed with a 7.0 T horizontal bore MRI scanner (BioSpec 70/20 Bruker Biospin, Billerica, MA, USA) equipped with a circularly polarized ^{1}H transmit/receive volume coil (inner diameter (ID) = 40 mm), with a maximum slew rate of 3458 T/m/s and maximum gradient strength of 446.4 mT/m.

2.2.1. Flow phantoms experiments

To evaluate the feasibility of the interstitial flow velocity-MRI sequence for measuring the low velocities of 10–500 μm/s, we constructed a flow phantom (Fig. 2A and B), using a 10 mL syringe (ID = 14.89 mm, Corning Co., Ltd.), a 50 mL centrifuge tube (ID = 26.5 mm, Corning Co., Ltd.), a hard rubber tube (ID = 2 mm, outer diameter (OD) = 6 mm, length = 4 m), and a controllable micro-injection pump (LSP01-1A Baoding Longer Precision Pump Co., Ltd.). The infusion pump was calibrated outside the magnet by weighing the infusate delivered at the set flow rate of 2 μL/min, which resulted in less than 10% errors. The rubber tube was inserted into a 50 mL centrifuge tube and then extracted parallelly. The centrifuge tube was filled with hydrogel to keep the rubber tube in place and remove air. The hydrogel formula: sodium alginate is prepared into a 3% solution with distilled water and placed in a constant temperature water bath at 60 °C so that it is completely dissolved. A 5% solution of anhydrous calcium chloride was prepared from distilled water. Add the calcium chloride solution by drops to the sodium alginate solution. In Fig. 2B, "+" indicates water flow entering, and "−" indicates water flow exiting. Thereafter, using a micro-injection pump with a controllable velocity, distilled water was injected into the rubber tube. This phantom provided an easily controlled fluid velocity as compared to interstitial flow velocity-MRI velocity measurements and directed subsequent *in vivo* experiments.

In this study, the flow imaging data for phantom was acquired for TE = 20.15 ms, repetition time (TR) = 3500.00 ms, flip angle (FA) = 90°, averages = 4, bandwidth = 300000.00 Hz, number of slices = 4, image size = 128 × 128, FOV = 40 mm × 40 mm, slice thickness = 1.00 mm, resolution = 0.313 mm × 0.313 mm, diffusion directions = 6, velocity directions = 3.

The theoretical flow rates (mean flow rates) were 2, 4, 10, 38, and 94 μL/min. The theoretical velocities (mean velocities) were 9.24, 23.10, 50.81, 203.24, and 498.85 μm/s. The *Venc* was 61.05, 81.4, 162.8, 651.2, and 976.8 μm/s.

2.2.2. Animal models experiments

All procedures involving animals in this study were performed in accordance with the ethical standards of the Institutional Animal Care and Use Committee of the National Center for Nanoscience and Technology and the 1964 Helsinki declaration and its later amendments or comparable ethical standard. BALB/c female mice, six to eight weeks old, were purchased from Beijing Vital River Laboratory Animal Technology Co., Ltd. (Beijing, China). The experimental mice used for the study were single-blind. Mouse 4T1 cells were cultured in Dulbecco's modified Eagle medium (DMEM) supplemented with 10% heated-inactivated Fetal Bovine Serum (FBS), penicillin (100 μg/mL), and streptomycin (100 μg/mL) at 37 °C and 5% CO_2. The 4T1 cell line used in this study was purchased from the Type Culture Collection (Chinese Academy of Sciences, Shanghai, China). BALB/c mice were inoculated with 4T1 tumour cells distally on the right thigh as 150 μL volume injections of 1×10^7 cells per mouse. This procedure has the following advantages. First, the distance from the heart and lungs can minimize the artifacts caused by heartbeat and breathing and facilitates fixing during the scanning process. Furthermore, the effect of injection on the life of mice can be minimized. Tumours were measured every two to three days using an electronic skin calliper from the longest width and length, and tumour volume was calculated as $4/3\pi r^3$, with the radius (r) calculated from tumour width and length measurement to provide an average diameter value. On the fifth day after tumour inoculation, mice were randomly divided into two groups of six. One group was administered losartan (40 mg/kg), and the other group was administered normal saline. There was no statistical difference in the mean tumour volume of mice in each group before administration. The experimental mice used in this study were not attrited, and all experiments were conducted according to the ethical principles of research (NCNST21-2011-0604). Losartan pills (Psaitong Biotechnology Co., LTD, LOT#: CSX16L1191KG, Renin-Angiotensin System Study, RRID: SCR_013385) were dissolved in Phosphate Buffered Saline (PBS) for 24 h. The solutions were then sterile filtered for injection. The duration of administration was ten days, once a day at a fixed time, and the method of administration was intraperitoneal injection.

Mice were anesthetized with 1%–1.5% isoflurane by inhalation and monitored during imaging for respiration. The mice were placed in the prone position and scanned using a T_2-weighted and interstitial flow velocity-MRI sequence. In this study, flow imaging data for mice were acquired for TE = 19.07 ms, TR = 14701.99 ms, FA = 90°, averages = 1, scan time = 11 min,

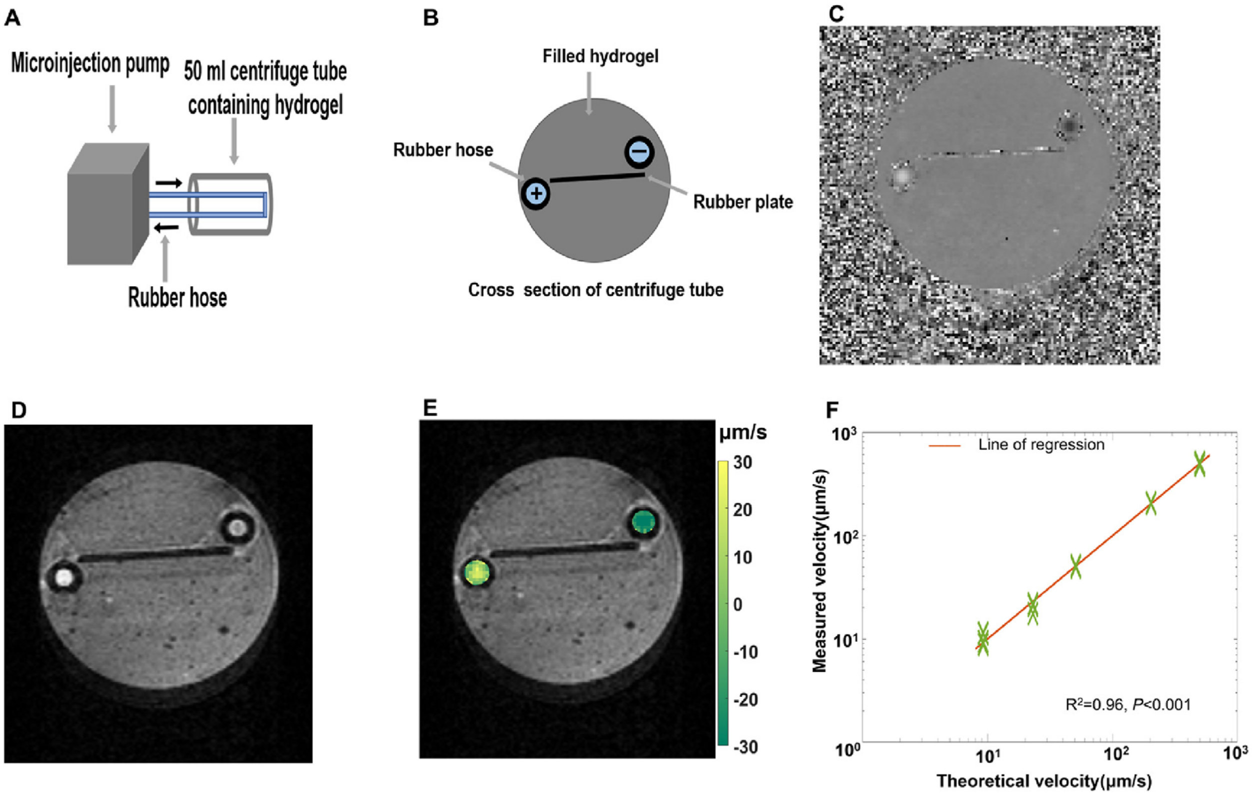

Fig. 2. Verify the feasibility of the interstitial flow velocity-MRI in the flow phantom. Schematic diagram of the flow phantom (A). The black arrow indicates the direction of water injection and output through the microsyringe pump. The cross-section of the 50 mL centrifuge tube and the rubber tube (B), filled with hydrogel, where the black "+" means water inflow, and the black "−" means water outflow. Phase image (C), representative amplitude image (D) and pseudo-color image (E) of the flow phantom cross-section. The theoretical velocity (mean velocity) and the *Venc* (C, D and E) were 9.24 μm/s and 61.05 μm/s. (F) The measurement velocity of the phantom is highly correlated with ($R^2 = 0.96$, $P < 0.001$) the theoretical velocity for *Venc* ranging from 60 to 1000 μm/s.

bandwidth = 200000.0 Hz, number of slices = 18, image size = 96 × 96, FOV = 30 mm × 30 mm, slice thickness = 1.00 mm, resolution = 0.313 mm × 0.313 mm, diffusion directions = 6, velocity directions = 3, max. *b* value = 25.51 s/mm^2, gradient amplitude (G) = ±20 mT/m, gradient duration (τ) = 3 ms, and time interval (Δ) = 100 ms, *Venc* = 651.2 μm/s.

After the scan, the mice were euthanized, and the tumour was removed, weighed, fixed, and sectioned. The number of EPI Imaging segments was eight, and echo spacing was 0.48 ms. $T_{1,\text{blood}}$ of 2190 ms was assumed, taken from the previous measurement on the 7T [27]. When partial saturation effects are accounted for, a more accurate representation of the inversion time that nulls the signal from the blood in an RF spin echo pulse (with TE « TR) sequence is shown in equation (8) [25].

$$TI = T_{1,\text{blood}} \ln\left(\frac{2}{1 + e^{\frac{-TR}{T_{1,\text{blood}}}}}\right). \tag{8}$$

For histopathological analysis, tumours from 4T1 tumour-bearing mice were harvested and fixed in 4% paraformaldehyde (Solarbio, China). Next, the samples were dehydrated using a graded series of alcohol, followed by embedding in paraffin wax (Leica, Germany, EG11). The samples were then sliced with a microtome (Leica, Germany, RM2245) and stained using Masson and Sirius red staining methods. Finally, ImageJ software was used for quantifying Masson- and Sirius red-positive areas (ImageJ, RRID:SCR_003070).

2.3. Statistical analysis

All images were processed using MATLAB (MATLAB, RRID:SCR_001622). All animal experiments were conducted with six mice in each treatment arm. Statistical analysis was performed with GraphPad Prism 8 (GraphPad Prism, RRID:SCR_002798). Pearson's correlations between theoretically set and measured velocities were calculated. All statistical analyses for the two groups were conducted using a *t*-test. *P* values < 0.05 and <0.01 were considered statistically different and significantly different, respectively. An asterisk indicates statistical significance in the figures.

3. Results

3.1. Low fluid velocity measurements in a homemade flow phantom

We generated a flow phantom (Fig. 2A and B) to simulate interstitial fluid flow and verify the feasibility and sensitivity of our MRI method (Fig. 1A). The theoretical velocities were estimated based on the known fluid inflow velocity, rubber tube diameter, and assumed laminar flow profiles.

When the *Venc* was in the range of 60–1000 μm/s, we found a significant correlation ($P < 0.001$, $R^2 = 0.96$) between theoretical and measured velocities (Fig. 2F). Our interstitial flow velocity-MRI successfully detected fluid flow velocity as low as 10.21 ± 2.65 μm/s (mean ± standard error) with a spatial resolution of 0.313 mm.

3.2. Interstitial fluid velocity in tumours

We evaluated 4T1 tumour-bearing mice ($n = 6$) using interstitial flow velocity-MRI. To generalise the results, the radial position (r/R) was normalized for the tumour radius [28]. First, we set the area with $0 < r/R \leq 0.5$ as the tumour centre and $0.5 < r/R \leq 1.0$ as the tumour margin. Next, we analysed interstitial fluid flow velocity in the tumour centre, tumour margin, and whole tumour, hypothesising that interstitial fluid flow velocity should differ across these parts (Fig. 3A). However, we did not find significant differences in flow velocity between the tumour centre and tumour margin or the whole tumour (Fig. 3B–D).

We depicted tumour interstitial fluid flow velocity using a pseudo-colour map (Fig. 4C and F) and calculated velocity distribution (Fig. 4G and H). We found that tumour interstitial fluid flow velocity ranged from 10 to 500 μm/s, with a mean value of 113 ± 24 μm/s (mean ± standard error). These flow velocity measurements are significantly greater than those obtained with conventional methods (0.1–55 μm/s) [7]. However, our results are close to the flow velocity values measured by Simon et al. using convection-MRI (10–220 μm/s) [17].

We used a streamlined algorithm to connect the flow path to show flow direction, creating an interstitial fluid velocity map (Fig. 4I and J). Surprisingly, fluid velocity magnitude and direction were more heterogeneous than speculated.

3.3. Effect of losartan on interstitial fluid velocity

We measured the magnitude and direction of interstitial fluid flow velocity in 4T1 tumour-bearing mice 10 days after losartan administration. The losartan group (40 mg/kg) had a lower ($P < 0.05$) mean (mean ± standard error) interstitial fluid flow velocity (85 ± 16 μm/s) than the control group (113 ± 24 μm/s) (0 mg/kg) (Fig. 5A–C) [29–31].

Collagen staining (using Masson and Sirius red) of extracted tumours showed that compared to the control treatment, losartan treatment significantly reduced the proportion of collagen fibres by 10% in the Masson staining group and by 12% in the Sirius red staining group (Fig. 5D–F).

4. Discussion

A new PC-MRI with ISTE was developed to measure interstitial fluid flow in phantom and 4T1 tumour-bearing mice. In this study, we used ISTE and increased the gradient interval Δ to minimize the *b*-value with the same flow measurement sensitivity, thus reducing signal loss caused by diffusion and improving the detection accuracy of slow-flow imaging. In addition, the phase error caused by gradient imperfection was reduced by using a bipolar gradient in the pulse sequence. This method can detect velocity as low as 10.21 ± 2.65 μm/s with a spatial resolution of 0.313 mm.

The mean velocity was 113 ± 24 μm/s and 85 ± 16 μm/s in the normal saline group and losartan treatment group, respectively; these values are higher than those recorded using other techniques. Munson et al. reviewed interstitial fluid velocity between 0.1 and 55 μm/s, measured in tumour mouse models and cancer patients, using a range of typical techniques [7]. Our results are close to the flow velocity values measured by Simon et al. using convection-MRI (10–220 μm/s) [17]. Since our technology can only measure velocity as low as 10.21 ± 2.65 μm/s, it is difficult to accurately measure the velocity that is lower than the detection sensitivity. In our *in vivo* measurements, fluid velocities greater than 55 μm/s may be due to contamination of faster-moving vascular fluid or necrotic areas. Therefore, we cannot claim that the velocity measurement comes entirely from the interstitium. In a follow-up study, we will look at sequence optimization and image post-processing to help realize the distinction between blood flow and interstitial fluid.

It has been reported that these mathematical models and the aforementioned experimental measurements are that peak velocities occur at the edge of the tumour, where the pressure gradient is steepest [32]. However, each of these mathematical models is limited by their specific assumptions of geometry and hydraulic properties of the tumour and the surrounding stroma, which strongly affect the predicted interstitial fluid velocity [7]. To explore whether the interstitial flow velocity has a similar trend, we divided it as shown in Fig. 3A but found no significant difference between the central and marginal flow velocity. We processed the interstitial velocity results and obtained a distribution map of flow velocity magnitude (Fig. 4G) and direction (Fig. 4I), indicating that interstitial fluid flow velocity is highly heterogeneous. As reported in many studies, flow patterns are a complex result of multiple factors, including transport between interstitial fluid and cells and transportation between blood and interstitial structures such as collagen fibres and hyaluronic acid. Although our results suggest that

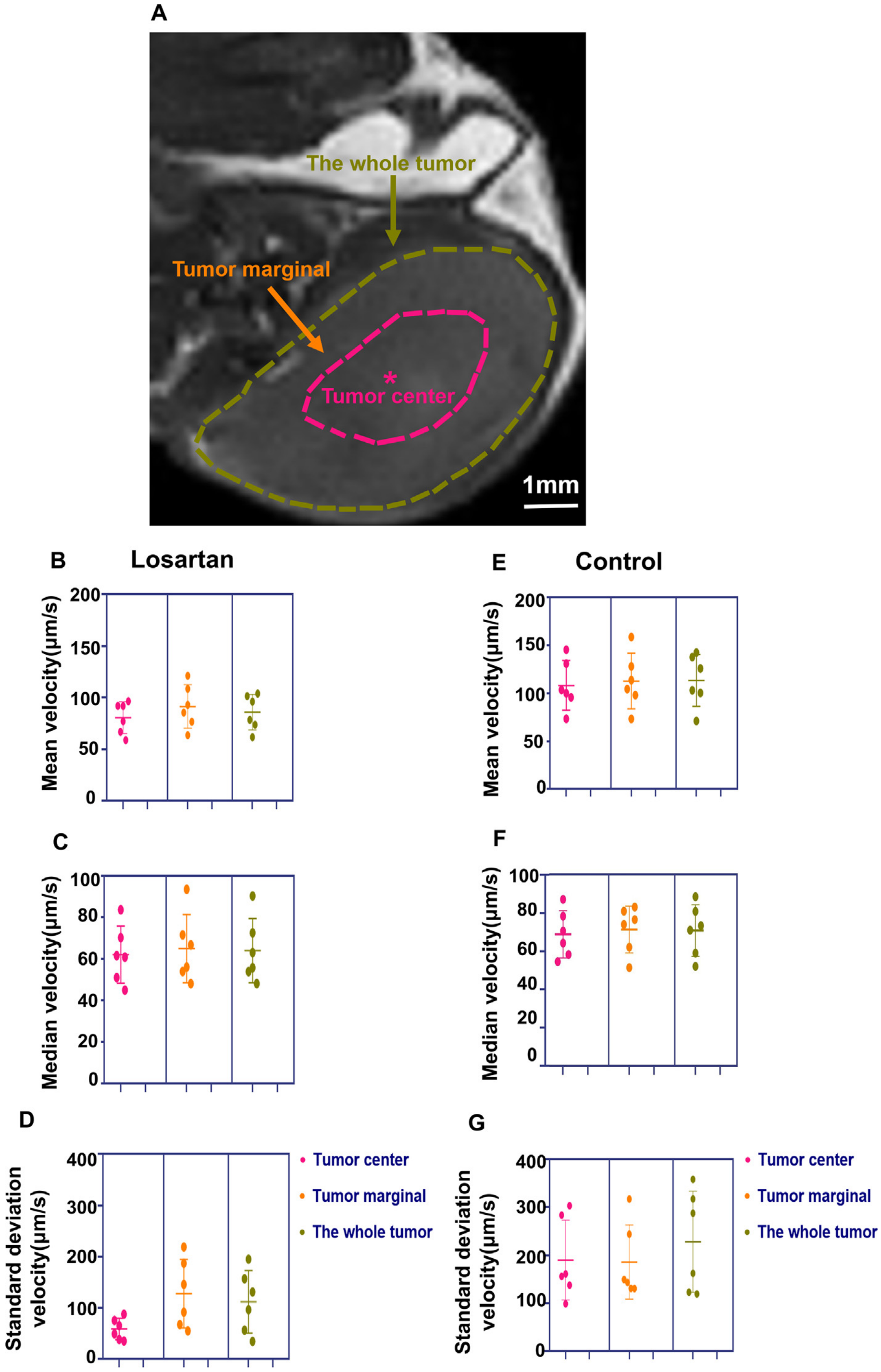

Fig. 3. Interstitial fluid flow velocity measured in the tumour center, tumour marginal, and the whole tumour. Representative image (A) of the tumour center (pink dotted line), tumour marginal (yellow arrow) and, the whole tumour (green dotted line). Mean velocity (B), median velocity (C), standard deviation velocity (D) in the tumour center, tumour marginal, and the whole tumour in the losartan treatment group. Mean velocity (E), median velocity (F), standard deviation velocity (G) in the tumour center, tumour marginal, and the whole tumour in the control group.

interstitial fluid flow is altered in the tumour microenvironment, they also highlight that the significant heterogeneity of the tumour and its microenvironment are not captured in a meaningful way.

Losartan is an angiotensin system inhibitor that reduces extracellular matrix content, leading to an anti-cancer effect [33–35]. Most available research investigating the impact of losartan on interstitial fluid emphasized on interstitial fluid

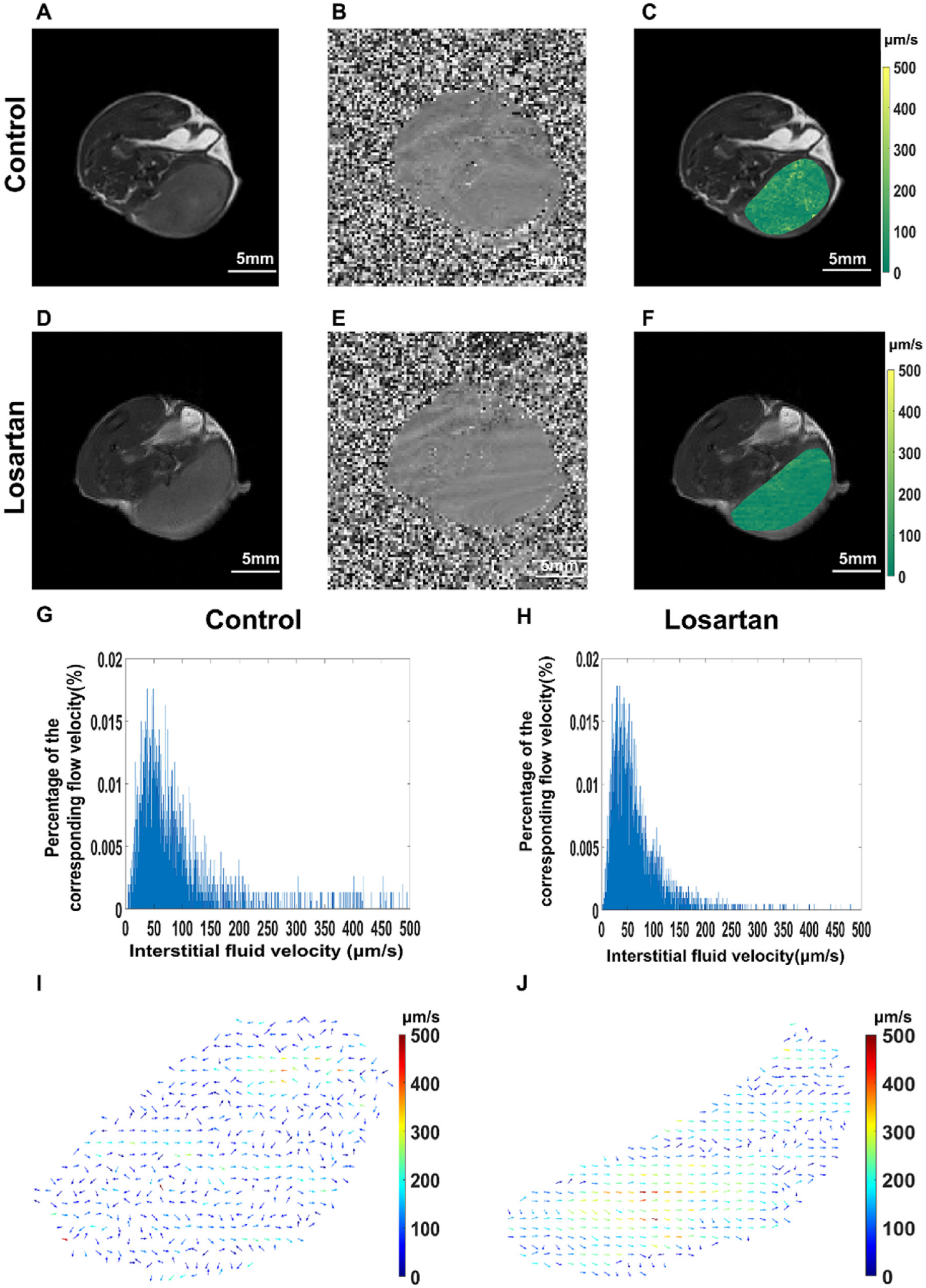

Fig. 4. Example interstitial flow velocity-MRI data set (raw image data and processed image data) in the 4T1 tumour bearing mice. Representative amplitude image (A), phase image (B), pseudo-color map (C) in the control group. Representative amplitude image (D), phase image (E), pseudo-color map (F) in the losartan treatment group. Histogram statistics of interstitial fluid flow velocity in the control group (G) and losartan treatment group (H). The color velocity vector diagram obtained by the streamlined algorithm shows the direction of interstitial fluid flow in the control group (I) and losartan treatment group (J).

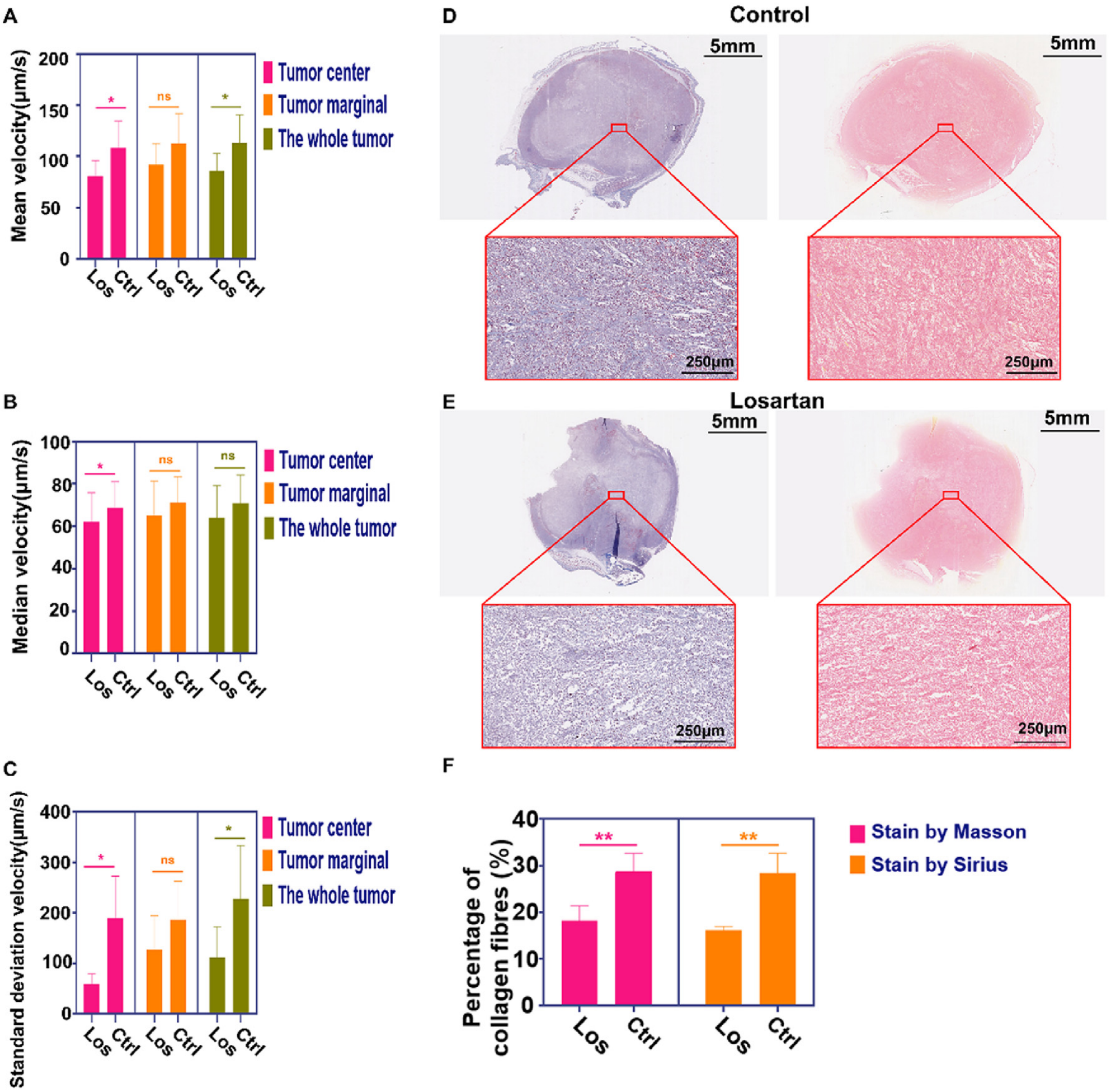

Fig. 5. Losartan targets the interstitial fluid flow velocity in the 4T1 tumour bearing mice. Mean (A), median (B) and standard deviation (C) of the interstitial fluid flow velocity in the center of the tumour, the edge of the tumour, and the entire tumour between the losartan treatment group and the control group. (*, $P < 0.05$. ns, not significant). Masson staining and Sirius staining of tumour tissues in the control group (D) and losartan treatment group (E). The difference in tumour collagen (F) between the control group and the losartan administration group (obtained by analyzing Masson staining and Sirius staining). (**, $P < 0.01$.)

pressure and tumour tissue blood perfusion [21–23,31]. However, the effect of losartan on tumour interstitial flow velocity had not been explored. Herein, we investigated the effect of losartan on the interstitial fluid flow velocity. We found that losartan inhibited collagen production, which is in agreement with previous studies. In addition, losartan negatively influenced tumour interstitial fluid flow velocity. Our study details the effect of losartan on the tumour microenvironment. However, the mechanism of losartan's effects on the interstitial flow velocity requires further exploration.

Our interstitial fluid imaging method is non-invasive and radiation-free. Therefore, it has potential applications in clinical imaging of tumour interstitial flow velocity. Currently, many interstitial fluid experiments are based on experimental animals. These tumours and their surrounding microenvironments may differ substantially from spontaneous human tumours, particularly when the immune system is compromised and cells are implanted in sites other than their tissue of origin [9,36]. These results are biased by using models of human cancer rather than naturally occurring human cancers. Therefore, the clinical application will require the determination of flow velocity ranges for human interstitial fluid. We should also consider appropriate experimental parameters such as field strength, FOV, and scan time. We believe that our novel method has great potential for improving cancer treatment. The phase errors caused by gradient field distortion become larger when it is used to measure high-precision velocity [37]. To improve the accuracy and robustness of the method, we need to introduce the elimination of factors affecting the image phase in future research [38]. Our method can be used to predict probable invasion areas and take proactive interventions because the interstitial fluid is closely linked to invasion and metastasis [7]. Moreover, velocity maps formulated with our MRI sequence are valuable for determining the relationship between disease progression and interstitial fluid flow changes.

5. Conclusion

We have developed a new technique for mapping mouse interstitial flow velocity. We tested this approach on 4T1 tumour-bearing mice and found high heterogeneity in the magnitude and direction of interstitial fluid flow velocity. Additionally, we found that losartan treatment reduced interstitial fluid velocity by inhibiting collagen production. Our findings reveal that interstitial flow velocity-MRI has the potential to rapidly screen drugs that alter interstitial fluid flow, as well as to predict tumour invasion area and evaluate treatment effects.

CRediT authorship contribution statement

Jun Zhao: Conceptualization, Methodology, Software, Validation, Formal analysis, Investigation, Data curation, Writing – original draft, Visualization. **Yupeng Cao:** Conceptualization, Methodology, Validation, Investigation, Writing – review & editing. **Wentao Liu:** Conceptualization, Methodology, Writing – review & editing, Supervision. **Dong Han:** Conceptualization, Methodology, Writing – review & editing, Supervision.

Declaration of competing interest

The authors declare that they have no known competing financial interests or personal relationships that could have appeared to influence the work reported in this paper.

Acknowledgement

This work was supported by National Natural Science Foundation of China (NO.61971151).

References

[1] H. Wiig, M.A. Swartz, Interstitial fluid and lymph formation and transport: physiological regulation and roles in inflammation and cancer, Physiol. Rev. 92 (2012) 1005–1060.
[2] N.A. Bhowmick, E.G. Neilson, H.L. Moses, Stromal fibroblasts in cancer initiation and progression, Nature 432 (2004) 332–337.
[3] R.K. Jain, Transport of molecules in the tumour interstitium: a review, Cancer Res. 47 (1987) 3039–3051.
[4] C. Wong, T. Stylianopoulosb, J.A. Cui, J. Martinb, V.P. Chauhanb, W. Jiang, et al., Multistage nanoparticle delivery system for deep penetration into tumour tissue, Proc. Natl. Acad. Sci. U.S.A. 108 (2011) 2426–2431.
[5] V.P. Chauhan, R.K. Jain, Strategies for advancing cancer nanomedicine, Nat. Mater. 12 (2013) 958–962.
[6] V.P. Chauhan, T. Stylianopoulos, J.D. Martin, Z. Popovic, O. Chen, W.S. Kamoun, et al., Normalization of tumour blood vessels improves the delivery of nanomedicines in a size-dependent manner, Nat. Nanotechnol. 7 (2012) 383–388.
[7] J.M. Munson, A.C. Shieh, Interstitial fluid flow in cancer: implications for disease progression and treatment, Cancer Manag. Res. 6 (2014) 317–328.
[8] E.M. de Kruijf, J.G.H. van Nes, C.J.H.V. de Velde, H. Putter, V.T.H.B.M. Smit, G.J. Liefers, et al., Tumour-stroma ratio in the primary tumour is a prognostic factor in early breast cancer patients, especially in triple-negative carcinoma patients, Breast Cancer Res. Treat. 125 (2010) 687–696.
[9] S.R. Chary, R.K. Jain, Direct measurement of interstitial convection and diffusion of albumin in normal and neoplastic tissues by fluorescence photobleaching, Proc. Natl. Acad. Sci. U.S.A. 86 (1989) 5385–5389.
[10] A. Pluen, Y. Boucher, S. Ramanujan, T.D. McKee, T. Gohongi, E. di Tomaso, et al., Role of tumour–host interactions in interstitial diffusion of macromolecules: cranial vs. subcutaneous tumours, Proc. Natl. Acad. Sci. U.S.A. 98 (2001) 4628–4633.
[11] Q.A. Zhou, R. Wood, E.M. Schwarz, Y.J. Wang, L.P. Xing, Near-infrared lymphatic imaging demonstrates the dynamics of lymph flow and lymphangiogenesis during the acute versus chronic phases of arthritis in mice, Arthritis Rheum. 62 (2010) 1881–1889.
[12] K.M. Kingsmore, A. Vaccari, D. Abler, S.X. Cui, F.H. Epstein, R.C. Rockne, et al., MRI analysis to map interstitial flow in the brain tumour microenvironment, APL Bioeng 2 (2018), 031905.
[13] M.A. Christen, D. Schweizer-Gorgas, H. Richter, F.B. Joerger, M. Dennler, Quantification of cerebrospinal fluid flow in dogs by cardiac-gated phase-contrast magnetic resonance imaging, J. Vet. Intern. Med. 35 (2021) 333–340.
[14] C. Blatter, E.F.J. Meijer, A.S. Nam, D. Jones, B.E. Bouma, T.P. Padera, B.J. Vakoc, In vivo label-free measurement of lymph flow velocity and volumetric flow rates using Doppler optical coherence tomography, Sci. Rep. 6 (2016), 29035.
[15] M. Markl, A. Frydrychowicz, S. Kozerke, M. Hope, O. Wieben, 4D flow MRI, J. Magn. Reson. Imag. 36 (2012) 1015–1036.
[16] L.A. Rivera-Rivera, P. Turski, K.M. Johnson, C. Hoffman, S.E. Berman, P. Kilgas, et al., 4D flow MRI for intracranial hemodynamics assessment in Alzheimer's disease, J. Cerebr. Blood Flow Metabol. 36 (2016) 1718–1730.
[17] S. Walker-Samuel, T.A. Roberts, R. Ramasawmy, J.S. Burrell, S.P. Johnson, B.M. Siow, et al., Investigating low-velocity fluid flow in tumours with convection-MRI, Cancer Res. 78 (2018) 1859–1872.
[18] H.Z. Lu, P.C.M. van Zijl, A review of the development of Vascular-Space-Occupancy (VASO) fMRI, *Neuroimage* 62 (2012) 736–742.
[19] C.K. Macgowan, C.J. Kellenberger, J.S. Detsky, K. Roman, S.J. Yoo, Real-time fourier velocity encoding: an in vivo evaluation, J. Magn. Reson. Imag. 21 (2005) 297–304.
[20] Y.P. Cao, Y. Zhang, Y.Q. Wang, W.T. Liu, D. Han, Improved stimulated echo in diffusion magnetic resonance imaging: introducing a π pulse for SNR enhancement, Magn. Reson. Med. 81 (2019) 2905–2914.
[21] B. Diop-Frimpong, V.P. Chauhan, S. Krane, Y. Boucher, R.K. Jain, Losartan inhibits collagen I synthesis and improves the distribution and efficacy of nanotherapeutics in tumors, Proc. Natl. Acad. Sci. U.S.A. 108 (2011) 2909–2914.
[22] V.P. Chauhan, J.D. Martin, H. Liu, D.A. Lacorre, S.R. Jain, S.V. Kozin, Angiotensin inhibition enhances drug delivery and potentiates chemotherapy by decompressing tumour blood vessels, Nat. Commun. 4 (2013) 2516.

[23] W. Li, S. Li, I.X. Chen, Y. Liu, R.R. Ramjiawan, C.H. Leung, et al., Combining losartan with radiotherapy increases tumor control and inhibits lung metastases from a HER2/neu-positive orthotopic breast cancer model, Radiat. Oncol. 16 (2021) 48.

[24] E. Haacke, R. Brown, M. Thompson, R. Venkatesan, Magnetic Resonance Imaging—Physical Principles and Sequence Design, John Wiley & Sons, New York, 1999.

[25] M.A. Bernstein, F.K. King, X.J. Zhou, Handbook of MRI Pulse Sequences, Elsevier Academic Press, Burlington. MA, 2004.

[26] W. Liu, X. Tang, Y. Ma, J.H. Gao, 3D phase unwrapping using global expected phase as a reference: application to MRI global shimming, Magn. Reson. Med. 70 (1) (2013) 160–168.

[27] S.D. Rane, J.C. Gore, Measurement of T1 of human arterial and venous blood at 7T, Magn. Reson. Imaging 31 (2013) 477–479.

[28] L.T. Baxter, R.K. Jain, Transport of fluid and macromolecules in tumours. i. Role of interstitial pressure and convection, Microvasc. Res. 37 (1989) 77–104.

[29] Y. Zhao, J. Cao, A. Melamed, M. Worley, A. Gockley, D. Jones, H.T. Nia, Y. Zhang, T. Stylianopoulos, A.S. Kumar, et al., Losartan treatment enhances chemotherapy efficacy and reduces ascites in ovarian cancer models by normalizing the tumor stroma, Proc. Natl. Acad. Sci. U.S.A. 116 (2019) 2210–2219.

[30] A. Hauge, E.K. Rofstad, Antifibrotic therapy to normalize the tumor microenvironment, J. Transl. Med. 18 (2020) 207–218.

[31] Y.X. Zhao, J.H. Cao, A. Melamed, M. Worley, A. Gockley, D. Jones, Losartan treatment enhances chemotherapy efficacy and reduces ascites in ovarian cancer models by normalizing the tumour stroma, Proc. Natl. Acad. Sci. U.S.A. 116 (2019) 2210–2219.

[32] J. Zhao, H. Salmon, M. Sarntinoranont, Effect of heterogeneous vasculature on interstitial transport within a solid tumor, Microvasc. Res. 73 (2007) 224–236.

[33] A. Hauge, E.K. Rofstad, Antifibrotic therapy to normalize the tumour microenvironment, J. Transl. Med. 18 (2020) 207.

[34] J.E. Murphy, J.Y. Wo, D.P. Ryan, J.W. Clark, W.Q. Jiang, Yeap BY, et al. Total neoadjuvant therapy with FOLFIRINOX in combination with losartan followed by chemoradiotherapy for locally advanced pancreatic cancer: a phase 2 clinical trial, JAMA Oncol. 5 (2019) 1020–1027.

[35] W.D. Li, S. Li, I.X. Chen, Y.J. Liu, R.R. Ramjiawan, C.H. Leung, et al., Combining losartan with radiotherapy increases tumour control and inhibits lung metastases from a HER2/neu-positive orthotopic breast cancer model, Radiat. Oncol. 16 (2021) 48.

[36] A. Clayton, Cancer cells use exosomes as tools to manipulate immunity and the microenvironment, OncoImmunology 1 (2012) 78–80.

[37] R. Lorenz, J. Bock, J. Snyder, J.G. Korvink, B.A. Jung, M. Markl, Influence of eddy current, maxwell and gradient field corrections on 3D flow visualization of 3D CINE PC-MRI data, Magn. Reson. Med. 72 (1) (2014) 33–40.

[38] S.Y. Ilik, T. Otani, S. Yamada, Y. Watanabe, S. Wada, A subject-specific assessment of measurement errors and their correction in cerebrospinal fluid velocity maps using 4D flow MRI, Magn. Reson. Med. 87 (5) (2021) 2412–2423.

Dong Han is a professor at the NCNST. After receiving his doctorate in basic medicine in 2001, he held a research position in the Department of Physics, Tsinghua University. In 2004, he established the Bio-imaging and Nanomedicine Laboratory at NCNST. He was a senior visiting scholar at École Normale Supérieure and Arizona State University. He has long been engaged in soft matter chemistry and medical research. He has made breakthroughs and original achievements in the fields of interstitial streams, living soft matter, biomechanopharmacology and hand-leading medicine.

Wentao Liu received his Ph.D. from Peking University. In 2016, he joined the research team led by Prof. Dong Han at the National Center for Nanoscience and Technology (NCNST) as an associate professor. His research interests cover the principles and imaging technologies of Magnetic Resonance Imaging (MRI), and the applications in nanomedicine.